Van Hove singularity and Lifshitz transition in thickness-controlled Li-intercalated graphene

S. Ichinokura,[1,*] M. Toyoda,[1] M. Hashizume,[1] K. Horii,[1] S. Kusaka,[1] S. Ideta,[2,3] K. Tanaka,[2] R. Shimizu,[4] T. Hitosugi,[4] S. Saito,[1,5,6] and T. Hirahara[1]

[1]*Department of Physics, Tokyo Institute of Technology, Tokyo 152–8551, Japan*
[2]*UVSOR Facility, Institute for Molecular Science, Okazaki 444–8585, Japan*
[3]*Hiroshima Synchrotron Radiation Center, Hiroshima University, Higashi-Hiroshima 739–8526, Japan*
[4]*Department of Applied Chemistry, Tokyo Institute of Technology, Tokyo 152–8550, Japan*
[5]*Advanced Research Center for Quantum Physics and Nanoscience, Tokyo Institute of Technology, Meguro-ku, Tokyo 152–8551, Japan*
[6]*Materials Research Center for Element Strategy, Tokyo Institute of Technology, 4259 Nagatsuta-cho, Midori-ku, Yokohama, Kanagawa 226–8503, Japan*

(Received 12 August 2021; revised 3 March 2022; accepted 2 June 2022; published 28 June 2022)

We demonstrate a method to control the Fermi level around the Van Hove singularity (VHS) in Li-intercalated graphene on the SiC substrate. By angle-resolved photoemission spectroscopy, we observed a clear Lifshitz transition in the vicinity of the VHS when the thickness of graphene exceeds four layers. We calculated the band structure of a multilayer system with different stacking sequences of graphene and Li layer. The so-called stage 2 model reproduces the Lifshitz transition, where Li occupies every other interlayer of graphene. In addition, we found that a sizable Schottky barrier is formed between graphene and the substrate. These properties allow us to explore the electronic phase diagram around the VHS by controlling the thickness.

DOI: 10.1103/PhysRevB.105.235307

Since the demonstration of superconductivity in twisted bilayer graphene [1], the many-body effect when the Van Hove singularity (VHS) is tuned at the Fermi level (E_F) has been intensively studied in two-dimensional materials [1–5]. In the twisting method, the moiré potential plays a vital role in forming a flat band. Another route to tune the VHS at E_F in graphene systems is heavy carrier doping by intercalation of guest metals [6–10]. It pulls down the native flat band around the saddle point (SP) of π band, initially located ∼2 eV above E_F, into an occupied state. A variety of electronic phases such as spin-density wave and unconventional superconductivity is predicted around VHS due to the enhancement of the strong correlation effect [11–15]. In Ca- [6], Gd- [10], Cs- [7], or Yb- [8,9] intercalated monolayer graphene, extended VHS [6–10] was observed, where the flat band is pinned to E_F in a wide range of wave-number space [6,8,9]. Compared to these examples, VHS in multilayer graphene is less established. This is because of the lack of basic information about multilayer intercalation systems, such as stage structure.

Li seems to be the best prototype intercalant for multilayer graphene because it is a cation of Li-ion battery with graphite electrodes. The thinnest case is Li-intercalated bilayer graphene, fabricated from epitaxial monolayer graphene on SiC by Li deposition [16–18]. Here, the buffer layer is lifted from the substrate and becomes the bottom graphene layer [19]. The resulting structure is C_6LiC_6/Li-terminated SiC, as shown in Figs. 1(a) and 1(b). The $\sqrt{3}\times\sqrt{3}R30^\circ$ superlattice of Li causes a periodic modulation called Kekulé-O type, which breaks the chiral symmetry of graphene [17,20]. A flat band near E_F was observed in the reports on bi- or trilayer Li-intercalated graphene [17,18,21]. However, no systematic study focused on VHS in Li-intercalated graphene with varying thickness. Moreover, the exact structure of the multilayer system has never been clarified.

In this work, we investigated the thickness dependence of the band structure of Li-intercalated graphene (LIG) with angle-resolved photoemission spectroscopy (ARPES) and density-functional theory (DFT) calculations. In the bilayer LIG/SiC, we observed a flat band at E_F, indicating the extended VHS. Surprisingly, we found that the SP robustly stays near E_F even if the thickness is increased, except for the slight shift when the thickness exceeds four layers. This results in a Lifshitz transition clearly seen at the Fermi surface. By DFT calculations for different models of the layered structure, we conclude that multilayer LIG/SiC is in stage 2 intercalation. Since Li only intercalates into every other graphene layer, the second Li layer intercalates only when there are four graphene layers. This results in the discrete transition of the doping level. We also performed DFT calculations including the substrate. It was clarified that the surface electronic state of Li-terminated SiC hybridizes with the Dirac band dispersion near the Fermi surface. A sizable Schottky barrier is also found between LIG and the substrate. These properties indicate the thickness-controlled LIG is promising to explore the transport properties under the correlation effect.

We prepared epitaxial graphene on the surface of an *n*-type Si-rich 4*H*-SiC(0001) single crystal by thermal decomposition in an Ar atmosphere. The thickness of graphene is controlled by optimizing the heating condition. The resulting thickness is evaluated from band dispersion at the $\bar{K}$ point, as shown in part SM-1 of Ref. [22]. Li was deposited

*ichinokura@phys.titech.ac.jp

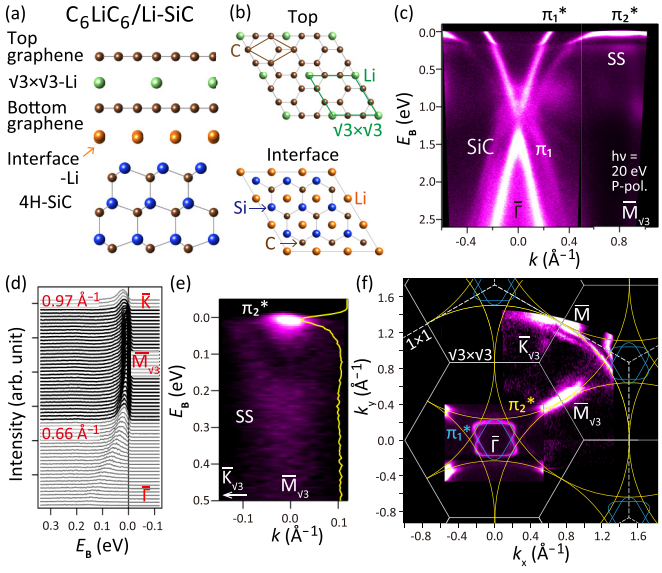

FIG. 1. (a), (b) Side (a) and top (b) view of the atomic model of C_6LiC_6/Li-SiC. (c)–(f) High-resolution ARPES data taken with p-polarized light at $h\nu = 20$ eV. (c) Band dispersion and (d) EDC mapping along the $\bar{\Gamma}$-$\bar{M}_{\sqrt{3}}$ direction. π_1, π_1^*, π_2^*, SS, and SiC bands are seen. SS and SiC bands are derived from surface and bulk state of the substrate, respectively. (e) Band dispersion along $\bar{M}_{\sqrt{3}}$-$\bar{K}_{\sqrt{3}}$ direction. The yellow line is the EDC at $k = 0$. (f) Fermi surface. The white dashed and solid lines indicate the boundary of 1×1 and $\sqrt{3}\times\sqrt{3}$ BZ, respectively. The blue and yellow solid lines are the guidelines for the contour of π_1^* and π_2^* band.

on graphene at room temperature from a resistively heated dispenser in an ultrahigh-vacuum chamber. The intercalation processing can be monitored in the electron-diffraction pattern. As written in Ref. [22], part SM-2, an n-1 layer graphene/buffer-terminated SiC turns into an n-layer LIG/Li-terminated SiC. Here, we use n ($n = 2$, 3, 4, and 5) to describe the number of graphene layers. We continued the deposition of Li until the intensity of $\sqrt{3}\times\sqrt{3}$ Li spots saturated to minimize the Li vacancy. ARPES measurements were performed *in situ* after the sample preparation with a commercial hemispherical photoelectron spectrometer equipped with angle and energy multidetections. We used two different apparatuses: Scienta Omicron R4000 in the lab with unpolarized HeIα (21.2 eV) radiation and MBS A1 at BL-7U of UVSOR-III using p- or s-polarized photons in the energy range of 14–40 eV [23]. The measurements were performed at room temperature in the lab and at 13 K in UVSOR (the data shown are taken at 13 K unless otherwise indicated).

In the $\sqrt{3}\times\sqrt{3}$ Brillouin zone (BZ), the $\bar{\Gamma}$ and $\bar{K}$ points of the 1×1 BZ are equivalent. Thus, we focus on the $\sqrt{3}\times\sqrt{3}$ BZ in this paper. The band structure of C_6LiC_6/Li-SiC along the $\bar{\Gamma}$-$\bar{M}_{\sqrt{3}}$ line is shown in Fig. 1(c). π_1, π_1^*, π_2^*, SS, and SiC bands are seen. SS and SiC bands are derived from the surface and bulk state of the substrate, respectively, as described later. A pair of Dirac cone π_1^* and π_1 has a gap of 0.37 eV, the same as reported in Ref. [17]. It is noteworthy that the π_2^*, the other Dirac band, has a flat dispersion near the Fermi energy at the $\bar{M}_{\sqrt{3}}$ point. As shown in the series of electron distribution curves (EDC) in Fig. 1(d), the flat band spans a wide range of wave numbers; from 0.66 to 0.97 Å^{-1}, the bandwidth is less than 10 meV. Such a flatness over a wide wave-number range is evidence of the extended VHS [6–10]. Since the flat band originates from the SP of graphene at the $\bar{M}$ point, it is electronlike in the orthogonal wave-number axis. Figure 1(e) shows that the bottom of the parabolic π_2^* band is located on E_F.

The Fermi surface is depicted in Fig. 1(f). In the first $\sqrt{3}\times\sqrt{3}$ BZ, both π_1^* and π_2^* approximately have a small and large hexagram contour centered at the $\bar{\Gamma}$ point (see the blue and yellow guidelines, respectively). Considering the BZ folding, the π_1^* hexagram is originated from triangular electron pockets at the $\bar{K}$ and $\bar{K}'$ point of the 1×1 BZ. π_2^* is a large circular hole pocket centered at the $\bar{\Gamma}$ point. From the volume of the Fermi surface, the carrier densities of π_1^* and π_2^* bands are estimated to be 1.4×10^{14} and 3.5×10^{14} cm^{-2}, respectively. The total is 4.9×10^{14} cm^{-2}, roughly consistent with the atomic density of $\sqrt{3}\times\sqrt{3}$ Li (6.3×10^{14} cm^{-2}). This implies that most of the electrons of $\sqrt{3}\times\sqrt{3}$ Li between graphene are transferred to the two graphene layers. There are also features near the $\bar{M}_{\sqrt{3}}$ point as discussed later.

Figures 2(a)–2(l) show the experimental band structures and the Fermi surfaces of n-layer LIG/Li-SiC with different thicknesses. The bands look pretty similar to C_6LiC_6/Li-SiC shown in Fig. 1. The most clearly resolved features are the electron band π_1^* and the hole band π_2^*. π_1 is a massive Dirac cone [Figs. 2(a), 2(c), and 2(e)]. By the numerical fittings described in Appendix A, we found that both the Dirac point (DP) and top of the π_1 band shift to the higher binding energy. The difference between them was 0.16 ± 0.01 eV irrespective of n, meaning no significant change in the gap size.

Figures 2(b), 2(d), and 2(f) show that the SP of π_2^* is located below the Fermi level for $n \geqslant 4$. Accordingly, as shown in Figs. 2(g)–2(l), the system exhibits a Lifshitz transition upon increasing thickness. The π_2^* Fermi surfaces touch each other at the $\bar{M}_{\sqrt{3}}$ points for $n \leqslant 3$, while they become separated for $n \geqslant 4$. We evaluated the carrier density of π_1^* and π_2^*, as shown in Fig. 2(m). In contrast to the slight expansion of π_1^*, π_2^* shows a discontinuous growth with the formation of the fourth layer and the Lifshitz transition.

To evaluate the binding energy of SP, we performed a parabolic fit on π_2^* along the $\bar{M}_{\sqrt{3}}$-$\bar{K}_{\sqrt{3}}$ direction, as shown in Figs. 2(j)–2(l). We plotted the binding-energy shift of the DP(SP) of experimental $\pi_1^*(\pi_2^*)$ bands as a function of the thickness in Fig. 2(n). One can see that SP hops from E_F to 50-meV higher binding energy at $n = 4$, following the Lifshitz transition. DP also shows rapid change up to $n = 4$ and takes constant value at 30 meV.

To look for the mechanism of the Lifshitz transition, we discuss the layered structure. Since the stage structure of multilayer LIG is unknown, we calculated band structures of n-layer LIG with stage 1 and 2 models using DFT calculations. For both models, the stacking manner of graphene is *AA* [24,25]. Li occupies the same hollow site between the graphene layers, i.e., Li atoms are aligned vertically [24,25]. Stage 1 is a state where Li fully intercalates to the graphene. In stage 2, Li occupies every other interlayer of graphene. The thermal stability of these structures is almost equal in

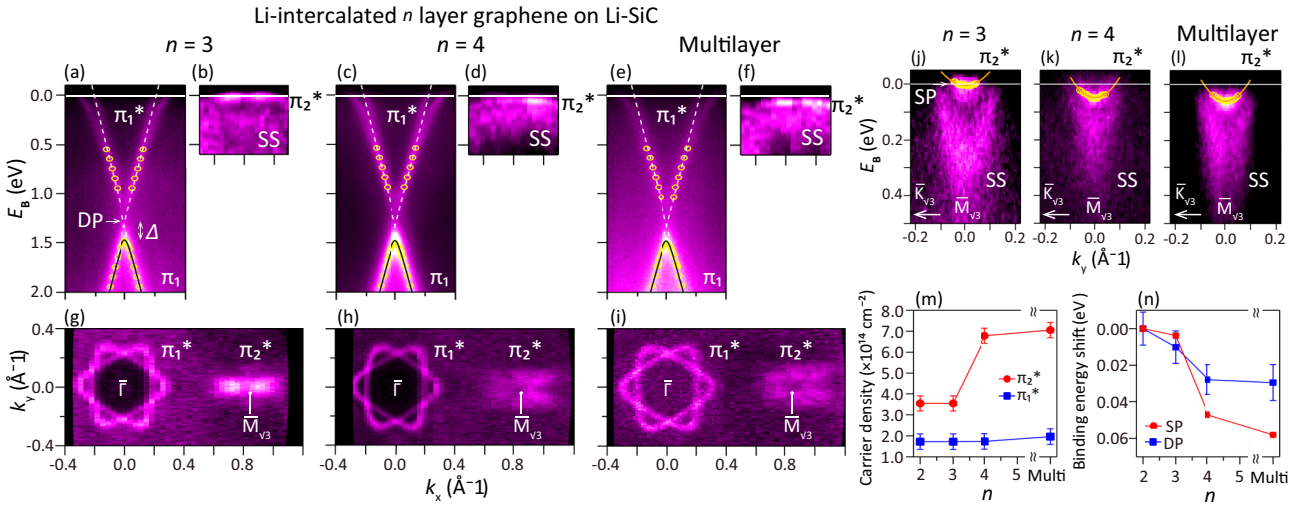

FIG. 2. Evolution of the band structure of n layer LIG/Li-SiC. (a)–(f) Band dispersion along the $\bar{\Gamma}$-$\bar{M}_{\sqrt{3}}$ direction. (a), (c), (e) and (b), (d), (f) show the data at the vicinity of the $\bar{\Gamma}$ and $\bar{M}_{\sqrt{3}}$ points, respectively. The yellow open circles represent the peak positions obtained by Lorentzian fitting to the raw ARPES spectra. The dashed white line is a linear fit of the dispersion. The solid black line is a fit by the massive Dirac cone equation to π_1 (see Appendix A). (g)–(i) Fermi contour. (j)–(l) Band dispersion along the $\bar{M}_{\sqrt{3}}$-$\bar{K}_{\sqrt{3}}$ direction. The yellow open circles are the same as (a), (c), and (e). The solid orange line indicates the parabolic fit to the peak positions. (m) Thickness dependence of the carrier density calculated from the volume of the Fermi surface. (n) Thickness dependence of the energy shift of the DP and SP. DP of π_1^* and SP of π_2^* are evaluated from the linear and parabolic fitting, respectively. All the data were taken with $h\nu = 21.2$ eV at room temperature.

bulk Li-intercalated graphite [26]. The computational details are described in Appendix B. Figure 3(a) displays the $n = 2$ case, namely C_6LiC_6, the band structures agree with π_1, π_1^*, and π_2^* in Fig. 1(c). We found that the occupied flat bands localize at the second graphene layer from the surface in $n \geqslant 3$, Ref. [22], part SM-3. Figures 3(b)–3(g) show the band

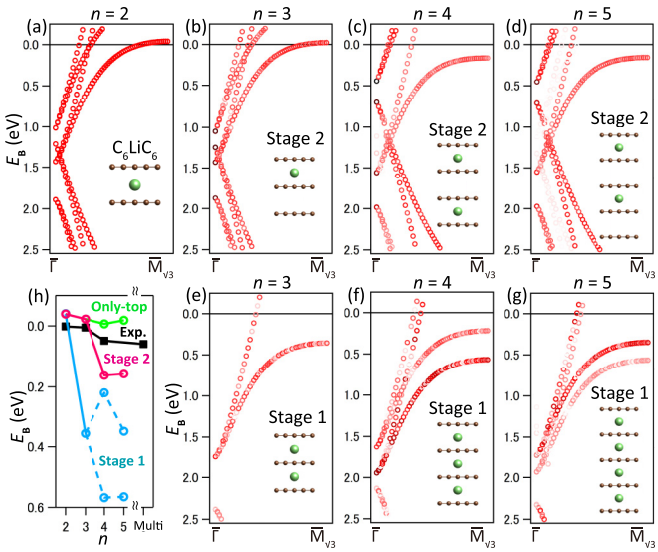

FIG. 3. (a)–(g) Band structure of the second layer of n layer LIG obtained by DFT calculations. (a) $n = 2$ (C_6LiC_6). (b)–(g) $n = 3$, 4, 5 in (b)–(d) stage 2 and (e)–(g) stage 1. The inset shows the schematic structure. (f) The binding energy of the flat band of the stage 1 (cyan), 2 (magenta), and top-intercalated (green) model comparing to the experiment (black) as a function of thickness. Note that in stage 1, the flat band splits into two branches when $n \geqslant 4$. This region is described by the dashed line.

structures of the second graphene layer in the stage 2 and 1 models with varying thickness. If we have a look at the evolution of band structure in stage 2 [Figs. 3(a)–3(d), upper panels], we notice that the flat band shifts from E_F to slightly below from $n = 3$ to 4. In stage 1 [Figs. 3(e)–3(g), lower panels], on the other hand, the flat band moves up and down because of the strong interlayer interaction. We can explain the transition in stage 2 by the structural change; due to the alternate intercalation of Li in stage 2, only one Li layer can be inserted up to $n = 3$. Here, the stacking is C_6LiC_6-C_6. Since the flat band is originated from the C_6LiC_6 part, it shows the same VHS as $n = 2$. When the thickness reaches $n = 4$, the second Li layer can penetrate as schematically drawn in the inset of Fig. 3(c). In this case, two C_6LiC_6 units have a weaker interaction than stage 1. It causes a small split to the C_6LiC_6 bands, resulting in a slight flat-band shift. We also calculated the band structure when only the top two layers of graphene are intercalated. As shown Ref. [22], the band structures of the top-intercalated model are almost identical to that of C_6LiC_6 and no Lifshitz transition was seen.

We summarized the binding energy of the flat band of the stage 1, 2, and top-intercalated model comparing to the experiment as a function of thickness in Fig. 3(h). The stage 1 and top-intercalation model are ruled out because the flat-band energy decreases too much or too less. Only the stage 2 model reproduces the abrupt transition at $n = 4$. Therefore, we conclude that multilayer LIG in the present experiment is in stage 2.

The difference in the magnitude of the band shift between the stage 2 model (0.2 eV) and the experiments (50 meV) remains an issue. Although we have not identified the reason, we found a factor to make the energy shift closer to the experiments by taking the substrate into account. Figure 1(c) shows some evidences of the substrate effect: the presence of

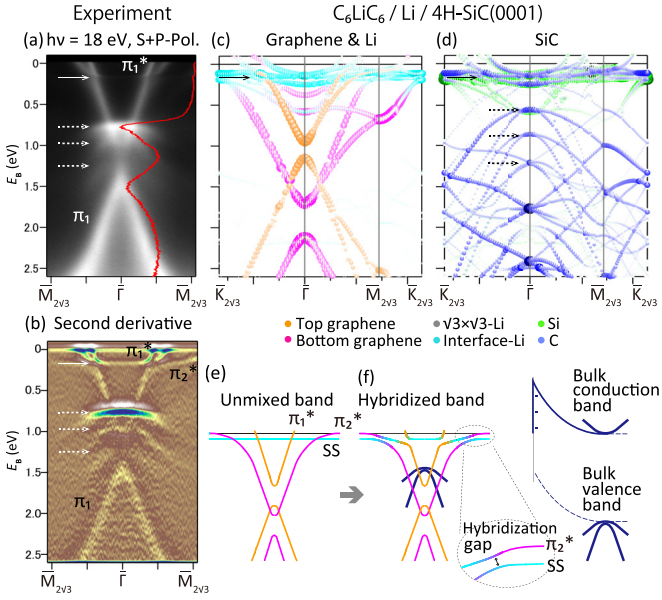

FIG. 4. (a) Sum of the ARPES intensity taken with p- and s-polarized light at $h\nu = 18$ eV around the $\bar{\Gamma}$ point. The solid red line is the EDC at the $\bar{\Gamma}$ point. (b) Second derivative of (a). (c), (d) Band structures calculated by DFT based on the model shown in Fig 1. (a), (b) Band structure is projected on C in top/bottom graphene (yellow/magenta), Li in $\sqrt{3}\times\sqrt{3}$/interface(gray/cyan), and Si/C(green/blue) in SiC. Both size and color of the dots are proportional to the projection of those atomic characters. In (a)–(d), solid and dashed arrows point out electronlike and holelike bands, corresponding to the surface and bulk band, respectively. (e), (f) Schematic illustration of the band hybridization and bending.

SS band, SiC band, and kink structures in π_1^* and π_2^*. They are more clearly seen by changing the energy and polarization of the incident light [22], part SM-4. Figure 4(a) shows the superposition of the spectra measured on C_6LiC_6/Li-SiC with s- and p-polarized light at $h\nu = 18$ eV. The electronlike band (solid arrows) and the holelike bands (dotted arrows) are observed. These structures are more accentuated by the second derivative, as shown in Fig. 4(b), indicating that the kink and the electronlike band are originated from the hybridization of two bands. We performed DFT calculations based on the structural model incorporating the substrate and interfaces as shown in Figs. 1(a) and 1(b). To reduce the calculation cost, we approximated the unit cell into $2\sqrt{3}\times 2\sqrt{3}$ $R30^\circ$ of graphene. The detail of the analysis is described in Appendix B.

The calculated results are shown in Figs. 4(c) and 4(d). The π_1^* and π_2^* bands are mainly composed of top and bottom graphene, respectively. One characteristic feature is the localized band at 0.2 eV, pointed out by solid black arrows. The main component is the surface state of Li-terminated SiC. Here, hybridization occurs at the crossing point of the Dirac cones and the localized bands. Figures 4(e) and 4(f) schematically illustrate the hybridization of those bands. The localized nature of the surface state at 0.2 eV is consistent with the SS band seen in Fig. 1(c). As schematically shown in Figs. 4(e) and 4(f), a hybridization gap opens between π_2^* and SS. This effect should also work in multilayer LIG, because SS was also seen in Figs. 2(b), 2(d), and 2(f). The binding energy of SS and the theoretically predicted flat-band shift in stage 2 are close to each other (0.2 eV). Therefore, we estimate that the hybridization suppresses the downward shift of the flat band when the layer number increases. In conclusion, the small shifting energy of the flat band at $n = 4$ results from a balance of interaction among C_6LiC_6 units and the substrate.

The holelike features around 0.7 eV are reproduced in Fig. 4(d) (pointed by black dashed arrows). Judging from the shape, they are the bulk bands of SiC [22], part SM-5. Here, the valence-band top should be located at around 3.2 eV deep inside the bulk since the substrate used in this study is degenerate. This means that considerable band bending (∼2.5 eV) occurs from the bulk towards the surface, forming a very high Schottky barrier. The magnitude of the bending is consistent with the reported core-level shift, interpreted to originate from the dipole layer at the Li–Si bonding [27].

In conclusion, we succeeded in the E_F tuning in n-layer LIG/Li-SiC by the thickness control, evidenced by the Lifshitz transition. By DFT calculations with and without substrate, we found that the stage 2 structure best reproduces the experimental band structure, including Lifshitz transition. We also found that Li intercalation between LIG and SiC naturally forms a sizable Schottky barrier. It will be interesting to identify the thickness dependence of the ground state in LIG on SiC due to the difference of the VHS position.

This work has been supported by Grants-In-Aid from Japan Society for the Promotion of Science (Grants No. 18H03877, No. 20H05183, No. 19K15443, No. 21K14533, and 19H01823), the Murata Science Foundation (Grants. No. H30-084 and No. H30-004), the Asahi Glass Foundation, the Sumitomo Foundation, Tokyo Tech. Challenging Research Award, and Tokyo Tech Advanced Researchers (STAR). The ARPES measurements were performed under the UVSOR Proposal No. 19–858, 20–777. A part of this work was conducted at NanofabPF, Tokyo Tech, supported by "Nanotechnology Platform Program" of the Ministry of Education, Culture, Sports, Science and Technology (MEXT), Japan, Grant No. JPMXP09F20IT0008. This work was partly supported by MEXT Elements Strategy Initiative to Form Core Research Center through Tokodai Institute for Element Strategy, Grant No. JPMXP0112101001.

APPENDIX A: ANALYSIS OF EXPERIMENTAL THICKNESS DEPENDENCE

Figures 2(a), 2(c), and 2(e) and 2(j), 2(k), and (l) in the main text are a series of the dispersion of π_1/π_1^* band at $\bar{\Gamma}$ point and of π_2^* band at $\bar{M}_{\sqrt{3}}$ points, respectively. From π_1 and π_1^*, we evaluated the energy of the Dirac point, the gap of the Dirac cone (Δ), and the Fermi velocity v_F. From π_2^*, we evaluated the saddle-point energy and effective mass m_e. The analysis of the values is conducted by the following method. The DP is defined by the crossing point of the linear functions fitted to the linear part of π_1 and π_1^* Dirac cone. The gap Δ is defined as the energy difference between DP and the top of the lower Dirac cone π_1. Δ can be estimated by the fitting of

TABLE I. Fermi velocity of $\pi_1{}^*$ and effective mass of $\pi_2{}^*$.

n	2	3	4	Multi
$v_F(\pi_1{}^*$, Linear)	6.24	6.26	6.00	5.90
[eV Å]	±0.09	±0.09	±0.07	±0.10
$v_F(\pi_1{}^*$, Dirac)	6.03	6.03	5.92	5.67
[eV Å]	±0.05	±0.09	±0.09	±0.07
m^*	0.8	0.8	0.52	0.50
($\pi_2{}^*$ Parabola)	±0.3	±0.1	±0.04	±0.03

the function

$$E = E_{DP} - \sqrt{\Delta^2 + (v_F k)^2} \tag{A1}$$

to the π_1 band, where the binding energy of Dirac cone E_{DP} is fixed to the value obtained from the linear fitting. Here, v_{F} is the Fermi velocity, which corresponds to the gradient of the Dirac cone outside of the gap. v_{F} estimated from two fittings [linear and using Eq. (A1)] are summarized in Table I. The SP is defined by the bottom of the π_2^* band at $\bar{\mathrm{M}}_{\sqrt{3}}$ point. Effective mass of π_2^* band is estimated by fitting to the parabolic function:

$$E = E_{SP} + \frac{(\hbar k)^2}{2m_e m^*}, \tag{A2}$$

where E_{SP} is the binding energy of the saddle point, $\hbar$ is the Dirac constant, and m_{e} is the electron mass. We summarized the constants obtained by these fitting in Table I. Compared to the Fermi velocity of π_1^*, the effective mass of π_2^* shows an abrupt change from $n = 3$ to 4, following the Lifshitz transition.

APPENDIX B: COMPUTATIONAL DETAILS

The electronic structure calculations were performed by using QUANTUM ESPRESSO package [28,29] within the framework of the Kohn-Sham DFT [30,31]. The calculations were performed in two steps: (1) model construction and (2) band-structure calculations. In the model construction step, the ultrasoft pseudopotentials [32] were used and the valance states were expanded in a plane-wave basis set with cutoff energies of 40 Ry for wave functions and 400 Ry for charge densities. In the band-structure calculation step, the norm-conserving pseudopotentials [33] and the cutoff energies of 120 Ry (wave functions) and 480 Ry (charge densities) were used. The electron-electron interaction was described within the local-density approximation [34]. An 8×8×1 k-point sampling mesh was used for integration over the Brillouin zone. The two-dimensional lattice parameters and the atomic positions were relaxed until the maximum force acting on atoms became less than 10^{-6} a.u. while the dimension along the c axis was kept constant at 40 Å (corresponds to the vacuum spacing wider than 20 Å). After the structural optimization, we performed the total energy comparison between different stacking patterns of the graphene layers, the Li atoms, and the substrate. We confirmed that the most stable structures have the AA-stacking graphene layers with the Li atoms intercalated at the hollow site of the graphene. To construct the model structure of C_6LiC_6/Li/4H-SiC(0001), we used the lattice matching of $2\sqrt{3}\times2\sqrt{3}$ graphene and 3 × 3 SiC(0001) instead of experimentally observed 13 × 13 graphene and $6\sqrt{3}\times6\sqrt{3}$ SiC(0001) for the sake of reducing computational cost. C_6LiC_6 is on the Si surface of the substrate while the C surface is terminated by hydrogen atoms. From the total energy comparison, we confirmed that the most favorable site of the (1 × 1) Li adatoms is the hollow site of SiC hexagons as shown in Table II. We then determined the stable position of C_6LiC_6 on the Li adatoms. The optimized structures of C_6LiC_6/Li/4H-SiC(0001) are shown in Figs. 1(a) and 1(b). Finally, we computed the band dispersions of these systems and analyzed them into the atom-decomposed band structure by taking the projection into the atomic orbitals.

TABLE II. Relative total energy of Li/4H-SiC(0001) with different Li positions.

Li site	hollow	ontop of Si	ontop of C
ΔE (eV/Li)	0	0.64	14.46

[1] Y. Cao, V. Fatemi, S. Fang, K. Watanabe, T. Taniguchi, E. Kaxiras, and P. Jarillo-Herrero, Nature (London) **556**, 43 (2018).

[2] M. Yankowitz, S. Chen, H. Polshyn, Y. Zhang, K. Watanabe, T. Taniguchi, D. Graf, A. F. Young, and C. R. Dean, Science **363**, 1059 (2019).

[3] X. Lu, P. Stepanov, W. Yang, M. Xie, M. A. Aamir, I. Das, C. Urgell, K. Watanabe, T. Taniguchi, G. Zhang *et al.*, Nature (London) **574**, 653 (2019).

[4] Y. Cao, V. Fatemi, A. Demir, S. Fang, S. L. Tomarken, J. Y. Luo, J. D. Sanchez-Yamagishi, K. Watanabe, T. Taniguchi, E. Kaxiras *et al.*, Nature (London) **556**, 80 (2018).

[5] A. L. Sharpe, E. J. Fox, A. W. Barnard, J. Finney, K. Watanabe, T. Taniguchi, M. A. Kastner, and D. Goldhaber-Gordon, Science **365**, 605 (2019).

[6] J. L. McChesney, A. Bostwick, T. Ohta, T. Seyller, K. Horn, J. González, and E. Rotenberg, Phys. Rev. Lett. **104**, 136803 (2010).

[7] N. Ehlen, M. Hell, G. Marini, E. H. Hasdeo, R. Saito, Y. Falke, M. O. Goerbig, G. Di Santo, L. Petaccia, G. Profeta *et al.*, ACS Nano **14**, 1055 (2019).

[8] P. Rosenzweig, H. Karakachian, D. Marchenko, K. Küster, and U. Starke, Phys. Rev. Lett. **125**, 176403 (2020).

[9] P. Rosenzweig, H. Karakachian, S. Link, K. Küster, and U. Starke, Phys. Rev. B **100**, 035445 (2019).

[10] S. Link, S. Forti, A. Stöhr, K. Küster, M. Rösner, D. Hirschmeier, C. Chen, J. Avila, M. C. Asensio, A. A. Zakharov *et al.*, Phys. Rev. B **100**, 121407 (2019).

[11] M. L. Kiesel, C. Platt, W. Hanke, D. A. Abanin, and R. Thomale, Phys. Rev. B **86**, 020507 (2012).

[12] W.-J. Lin, W. LiMing, and T. Zhou, Phys. Rev. B **103**, 174513 (2021).
[13] R. Nandkishore, L. S. Levitov, and A. V. Chubukov, Nat. Phys. **8**, 158 (2012).
[14] A. M. Black-Schaffer and C. Honerkamp, J. Phys.: Condens. Matter **26**, 423201 (2014).
[15] D. Makogon, R. van Gelderen, R. Roldán, and C. M. Smith, Phys. Rev. B **84**, 125404 (2011).
[16] S. Fiori, Y. Murata, S. Veronesi, A. Rossi, C. Coletti, and S. Heun, Phys. Rev. B **96**, 125429 (2017).
[17] C. Bao, H. Zhang, T. Zhang, X. Wu, L. Luo, S. Zhou, Q. Li, Y. Hou, W. Yao, L. Liu *et al.*, Phys. Rev. Lett. **126**, 206804 (2021).
[18] N. M. Caffrey, L. I. Johansson, C. Xia, R. Armiento, I. A. Abrikosov, and C. Jacobi, Phys. Rev. B **93**, 195421 (2016).
[19] F. Bisti, G. Profeta, H. Vita, M. Donarelli, F. Perrozzi, P. M. Sheverdyaeva, P. Moras, K. Horn, and L. Ottaviano, Phys. Rev. B **91**, 245411 (2015).
[20] O. V. Gamayun, V. P. Ostroukh, N. V. Gnezdilov, İ. Adagideli, and C. W. J. Beenakker, New J. Phys. **20**, 023016 (2018).
[21] K. Sugawara, K. Kanetani, T. Sato, and T. Takahashi, AIP Advances **1**, 022103 (2011).
[22] See Supplemental Material at http://link.aps.org/supplemental/10.1103/PhysRevB.105.235307 for detailed information about the growth method of graphene with thickness control, comparison of electron-diffraction pattern before and after Li deposition, comprehensive results of the DFT calculations and photon energy-dependent ARPES, and additional information of bulk band structure of SiC.
[23] S.-I. Kimura, T. Ito, M. Sakai, E. Nakamura, N. Kondo, T. Horigome, K. Hayashi, M. Hosaka, M. Katoh, T. Goto *et al.*, Rev. Sci. Instrum. **81**, 053104 (2010).
[24] M. S. Dresselhaus and G. Dresselhaus, Adv. Phys. **51**, 1 (2002).
[25] S. N. Shirodkar, M. Mattheakis, P. Cazeaux, P. Narang, M. Soljačić, and E. Kaxiras, Phys. Rev. B **97**, 195435 (2018).
[26] W. Zhou and P. H. L. Sit, ACS Omega **5**, 18289 (2020).
[27] C. Virojanadara, S. Watcharinyanon, A. A. Zakharov, and L. I. Johansson, Phys. Rev. B **82**, 205402 (2010).
[28] P. Giannozzi, S. Baroni, N. Bonini, M. Calandra, R. Car, C. Cavazzoni, D. Ceresoli, G. L. Chiarotti, M. Cococcioni, I. Dabo *et al.*, J. Phys.: Condens. Matter **21**, 395502 (2009).
[29] P. Giannozzi, O. Andreussi, T. Brumme, O. Bunau, M. Buongiorno Nardelli, M. Calandra, R. Car, C. Cavazzoni, D. Ceresoli, M. Cococcioni *et al.*, J. Phys.: Condens. Matter **29**, 465901 (2017).
[30] P. Hohenberg and W. Kohn, Phys. Rev. **136**, B864 (1964).
[31] W. Kohn and L. J. Sham, Phys. Rev. **140**, A1133 (1965).
[32] A. M. Rappe, K. M. Rabe, E. Kaxiras, and J. D. Joannopoulos, Phys. Rev. B **41**, 1227(R) (1990).
[33] N. Troullier and J. L. Martins, Phys. Rev. B **43**, 1993 (1991).
[34] J. P. Perdew and A. Zunger, Phys. Rev. B **23**, 5048 (1981).